Applied Energy 260 (2020) 114252

Contents lists available at ScienceDirect

Applied Energy

journal homepage: www.elsevier.com/locate/apenergy

Experimental investigation on the hydrodynamic performance of a cylindrical dual-chamber Oscillating Water Column device

De-zhi Ning[a,*], Yu Zhou[a], Robert Mayon[a], Lars Johanning[a,b]

[a] State Key Laboratory of Coastal and Offshore Engineering, Dalian University of Technology, Dalian 116024, China
[b] College of Engineering, Mathematics and Physical Sciences, University of Exeter, Penryn Campus, Penryn, Cornwall TR10 9FE, UK

HIGHLIGHTS

- An experimental study on a cylindrical dual-chamber OWC device was carried out.
- The outer chamber can improve the hydrodynamic performance of the OWC device.
- There exist two different resonant frequencies in the inner- and outer- chambers.
- The hydrodynamic efficiency of the device decreases as the wave steepness increases.

ARTICLE INFO

Keywords:
Oscillating water column
Cylindrical dual-chamber
Hydrodynamic efficiency
Air pressure
Physical experiment

ABSTRACT

The hydrodynamic performance of a stationary cylindrical dual-chamber Oscillating Water Column (OWC) wave energy device was experimentally studied to assess conversion efficiency in comparison with a single-chamber OWC. The contribution of the present work is to guide the design and optimization of the dual-chamber OWC device for efficiently capturing offshore wave energy. The effects of various parameters including wave steepness, the opening ratio, the inner- and outer-chamber drafts on the hydrodynamic efficiency of the proposed OWC device were considered. It was found that the hydrodynamic efficiency of the dual-chamber OWC device increases by comparison with the single-chamber one. A coupled resonant effect between the inner- and outer-chambers was observed for the dual-chamber OWC, which leads to the difference between the resonant frequencies and broadens the effective frequency bandwidth. The ratio of the orifice opening area to the area of the chamber columns has a significant influence on the hydrodynamic efficiency. The optimal opening ratio is founded to be between 1.5% and 2.0% in the present study. It was also observed that the hydrodynamic efficiency decreases with the increase of wave steepness and increases with the decrease of the outer-chamber draft.

1. Introduction

Renewable energy has been widely recognized as the optimal choice to cope with the increasing costs of fossil fuels [1]. In addition, recent renewable energy policies have gained much societal support as the means to mitigate environmental pollution arising from fossil fuel usage to support economic development [2]. Ocean wave energy, which possesses a high power intensity flow (2–3 kW/m^2), has gained attention as an important source of renewable wave energy [3]. A great number of technological concepts have been developed to extract ocean energy, such as the Pelamis [4], Oscillating buoys [5], and enclosed chambers [6]. Among the various concepts, the Oscillating Water Column (OWC) type wave energy converter (WEC) has been widely investigated and applied since its first development as an audible navigation aid [7]. Moreover, a number of prototypes of the concept OWC devices have been constructed. The water column inside the chamber is excited by the incident waves and oscillates like a piston to generate pneumatic air. A power take-off (PTO) turbine is driven by the pneumatic air to generate the electricity [8]. Due to their uncomplicated designs and low-cost, many government- and commercially-funded programmes have encouraged researchers to further examine OWC type devices, especially through prototype tests at sea, such as the Pico plant (400 kW) in Portugal [9], the Oceanlinx MK3 (2.5 MW) in Australia [10], the Islay plant (500 kW) in Scotland [11], the Shanwei OWC plant (100 kW) in Guangdong, China [12], and the onshore Mutriku and offshore Oceantec OWC technologies demonstrated in Spain [13].

For the preliminary study and design of OWC devices, the linear

* Corresponding author.
E-mail address: dzning@dlut.edu.cn (D.-z. Ning).

https://doi.org/10.1016/j.apenergy.2019.114252
Received 26 August 2019; Received in revised form 20 November 2019; Accepted 23 November 2019
Available online 09 December 2019
0306-2619/ © 2020 The Authors. Published by Elsevier Ltd. This is an open access article under the CC BY-NC-ND license (http://creativecommons.org/licenses/BY-NC-ND/4.0/).

potential-flow theory has generally been adopted to describe the physical process of energy conversion; see for example Garrett [14], Sarmento and Falcão [15] and Evans and Porter [16]. Even though the linear potential-flow theory can estimate the resonant frequency of wave-WEC interaction efficiently, it is not able to describe the exact behaviour of the fluid due to the omitted terms describing the fluid viscosity and wave nonlinearity in the governing equations. A wide variety of OWC analytical models have also been proposed and developed to describe the energy capture capability of the devices. Zheng et al. [17] investigated the effects of geometric parameters on the hydrodynamic properties of a coast/breakwater-integrated OWC device. Zheng et al. [18] also developed a linear radiation and diffraction model to simulate an array of OWC devices, which were installed on a straight coastline. Due to the effects of constructive wave interference from the array layout and the coast, the hydrodynamic efficiency of the OWC devices in the array was enhanced significantly for the certain range of wave conditions. Martin-Rivas and Mei [19] developed a linear radiation and diffraction model to simulate a cylindrical OWC device which was installed on a straight coast. Due to the coastal reflection, the observed capture efficiency was 2–3 times greater than that of an isolated offshore OWC device. Rezanejad et al. [20] investigated the hydrodynamic properties of an OWC device with an artificial stepped seabed topology. It was found that by optimising the certain spatial parameters of the artificial step, an increase in the capacity of wave power absorption could be achieved. Deng et al. [21] derived an analytical model for a cylindrical OWC device with a V-shaped inlet channel. The V-shaped channel significantly increases the conversion efficiency and broadens the effective frequency bandwidth. Ning et al. [22] simulated a 3D, floating dual-chamber OWC-WEC using an analytical approach. It was discovered that the peak hydrodynamic efficiency and the effective frequency bandwidth are enhanced by introducing an outer-chamber shell.

Advanced numerical models have also been widely used for simulating the complex interactions between ocean waves and OWC devices. Based on potential flow theory, OWC computational models employing the Finite Element Method (FEM) and Boundary Element Method (BEM) were developed. Nader et al. [23] developed a FEM model to investigate the scattered waves around single and multiple oscillating water column wave energy conversion devices. Based on linear potential theory and experimental methods, Gomes et al. [24] analyzed the effects of the tank wall on the hydrodynamics of a heaving Spar-buoy OWC device in a channel. A higher-order BEM model was also developed to study the hydrodynamic efficiency of a 2D onshore dual-chamber OWC-WEC by Ning et al. [25]. Compared with the single-chamber device, the dual-chamber OWC device displayed a higher hydrodynamic efficiency near the resonant frequency. A number of viscous-flow models were also developed to accurately simulate the viscous losses and vortex shedding at the OWC device. López et al. [26] developed a 2D CFD model to analyse the turbine damping at the orifice of an OWC device under regular and irregular wave conditions. Based on the Navier-Stokes equations and the Volume of Fluid (VOF) method, Elhanafi et al. [27] performed a 3D CFD investigation of the effects of model scale and air compressibility on the OWC energy conversion. Xu and Huang [28] developed a CFD numerical wave flume using an OpenFOAM library to study a bottom-fixed cylindrical OWC-WEC. However, the viscous-flow models are time-consuming at the present stage and they still require validation through the physical experiments.

A large number of experimental investigations have been undertaken to study the hydrodynamics of OWC-WECs. Çelik and Altunkaynak [29] carried out a flume experiment on a rectangular bottom-fixed OWC model, which was used to validate a mathematical vibration model. Wilbert et al. [30] used an experimental approach to study the hydrodynamic properties of a 2D Dual-Chamber Oscillating Water Column (DCOWC). It was found that the hydrodynamic efficiency of the DCOWC was nearly 10% higher than that of a Single-Chamber Oscillating Water Column (SCOWC). Moretti et al. [31] performed a small-scale physical experiment on an OWC designed with a U-shaped collector. The effect of the PTO system on the dynamical response of the OWC system is investigated in depth. A large-scale physical experiment on the integration of an OWC-WEC device into a breakwater caisson was also carried out by Pawitan et al. [32]. In their study, the pressure distributions and the wave loads on the caisson chamber were measured in both regular and irregular wave conditions. Xu et al. [33] investigated the hydrodynamics of a cylindrical shoreline OWC device with a quadratic PTO model using both experimental and theoretical approaches. The effects of various environmental parameters (including non-linear PTO damping, fluid viscosity and spatial non-uniformity inside the OWC chamber etc) were examined. Mahnamfar and Altunkaynak [34] optimized an onshore fixed OWC device to obtain the maximum captured power by experimental and numerical methods. They found that the hydrodynamic efficiency of the modified OWC device was increased by 80% compared with the classical OWC device.

The construction of an onshore OWC device is severely restricted by the coastline morphology unless the OWC is integrated into a breakwater or other floating structure [35]. However, in contrast to onshore or nearshore OWC devices, where the chamber rear wall forms part of the shoreline or it extends to the seabed, the offshore floating OWC device, has all its walls detached from the seabed [36]. This allows ocean waves to pass underneath and around the device, and thus it can capture energy from multiple wave directions. Because of this reduced wave direction dependence, offshore floating OWCs can achieve a high level of energy flow density. Most previous researches have focused on the single–chamber OWC devices [37] wherein the performance of the devices is optimal at a wave period coinciding with the chamber resonance frequency. He et al. [38] studied the hydrodynamic properties of a dual-chamber OWC, which was integrated into a floating breakwater. It was observed that floating breakwaters with asymmetric OWC chambers broadens the efficient operational frequency bandwidth. Sheng et al. [39] designed and tested a cylindrical floating OWC with mooring lines in both regular and irregular waves. Their study found that the motion response of the floating OWC-WEC was not significantly affected by varying the PTO damping. Elhanafi et al. [40] carried out an experiment to study the hydrodynamic properties of an offshore floating–moored OWC wave energy converter. The simulated results show that the hydrodynamic efficiency increases as the in-phase moment occurs between surge motion of the device and the oscillation of the chamber colume. Correia et al. [41] analysed the performance of a connected three-device OWC triangular array of spar-buoys. It was found that the array arrangement of the spar-buoy performs better than a single device. Louise et al. [42] carried out an experiment on an array of five OWC-WECs to investigate the effects of wave disturbance. They found that the radiation waves induced by the oscillating water column have a significant effect on the local wavefield adjacent to the array layout.

Based on the previous researches of the onshore/nearshore dual-chamber OWC devices, the hydrodynamic performance can be improved apparently by comparison with the single-chamber ones. However, the relating works on the offshore dual-chamber OWC-WEC are still scarce, especially for 3D experimental investigations. Thus, the primary objective of the present work is to provide useful guidance and evaluation for the design of a cylindrical dual-chamber OWC-WEC through an experimental approach. The effects of wave nonlinearity, the orifice scale and the sub-chamber draft on the hydrodynamic efficiency, the free-surface motion and air pressure inside the chamber, are considered. The rest of the paper is organized as follows: The experimental procedure is described in Section 2. Experimental results are compared with the analytical solutions in Section 3. In Section 4, the differences between the dual-chamber and single-chamber OWC devices are presented. The effects of the wave steepness, the opening ratio and sub-chamber drafts on the hydrodynamic performance of the dual-chamber OWC device are discussed. Finally, the conclusions of this

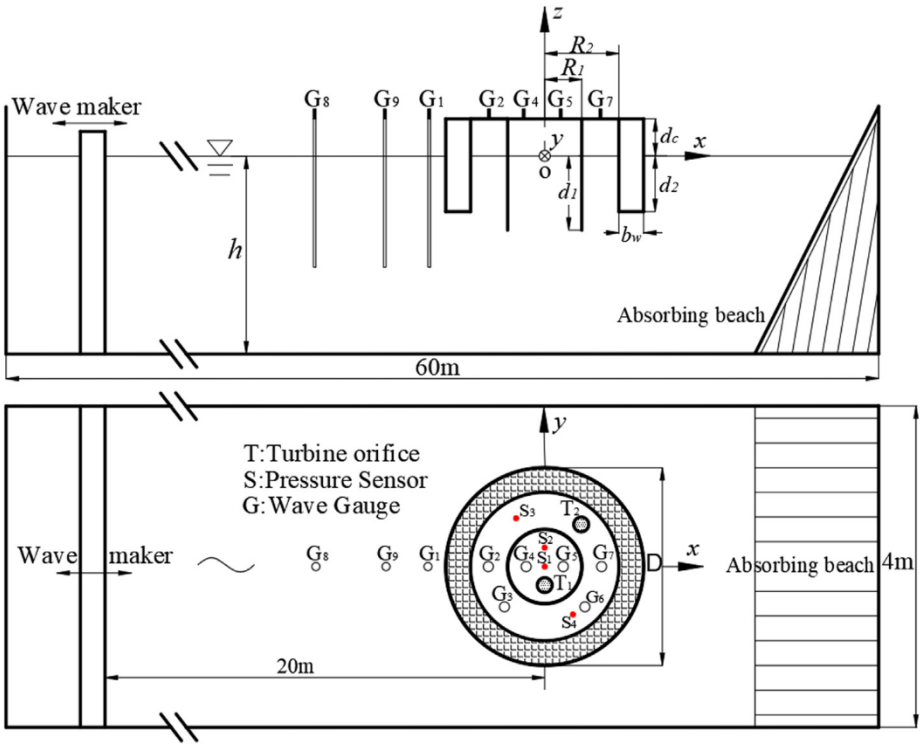

Fig. 1. Experiment layout. Top: a side view showing the OWC device and the wave gauges; Bottom: a plan view of the orifices and the pressure sensors.

Fig. 2. View of the (a) dual-chamber OWC and (b) single-chamber OWC with 1:20 scale model.

study are summarized in Section 5.

2. Experiment

2.1. Experiment setup

The experimental investigations were carried out in the wave-current flume at the State Key Laboratory of Coastal and Offshore Engineering, Dalian University of Technology, China [43]. The wave-current flume is 60 m long, 4 m wide and its maximum water depth is 2.5 m. A piston-type wave-maker located at one end of the wave-current flume can generate waves with periods ranging from 0.5 s to 5.0 s. An artificial damping beach is located at the other end of the flume. The OWC model with a 1:20 scale was installed at the centerline of the flume and 20 m away from the wave maker (see Fig. 1). Fig. 1 shows the sketch of the wave flume and the experimental setup. The dual-chamber OWC-WEC is fixed on the free surface. A Cartesian coordinate system O*xyz*, with the origin O is defined at the axisymmetric center of the dual-chamber OWC-WEC, *x*-axis positive in the direction of incident wave propagation, and *z*-axis positive upward, as shown in Fig. 1. The static water depth h is 1.0 m, with the inner-chamber radius $R_1 = 0.15$ m and the outer-chamber radius $R_2 = 0.3$ m. The inner-wall thickness is 0.008 m. The outer-wall thickness $b_w = 0.1$ m. Because the outer wall is hollow, it can provide buoyancy for the complete device. In this study the inner- and outer-chamber walls are named as Shell-1 and Shell-2 respectively. The effect of the lateral flume-walls are ignored as the ratio of the flume width (B) to the model diameter (D) is 5 [44]. The drafts of the inner- and outer-chambers are defined as d_1 and d_2 respectively. The thickness of the chamber ceiling plate is 16 mm. There are two circular orifices (i.e., T_i and T_o, where the subscripts i and o denote the inner and outer chamber respectively.) on the ceiling of the inner- and outer-chambers, which are used to simulate the PTO

Table 1
Geometric parameters used in the experiments.

Opening ratio ε	Diameter of T1	Diameter of T2	Draft d_1	Draft d_2	Draft d_{single}
1.0%	30 mm	52 mm	0.42 m	0.4 m	0.42 m
1.5%	36 mm	64 mm	0.37 m	0.35 m	–
2.0%	42 mm	75 mm	0.32 m	0.3 m	–
3.0%	52 mm	90 mm	0.27 m	–	–

system [45]. The locations (x, y, z) of the circular orifices are positioned at T_i (0 m, −0.075 m, 0.1 m) and T_o (0.16 m, 0.16 m, 0.1 m). In the present study, four different opening ratios ε ($\varepsilon = S_0/S$, where S_0 and S are the cross-sectional areas of the circular orifice and the circular chamber, respectively [40]) are examined. A single-chamber OWC device with the same geometrical dimensions as the inner-chamber of the dual-chamber OWC (shown in Fig. 2(b)) is also studied to compare the experimental results. The effects of supplementary floaters to aid the buoyancy of the chamber is not considered. The draft of the single-chamber OWC model is $d_{single} = 0.42$ m. The single-chamber wall thickness is $b_{single} = 0.008$ m. The radius of the single-chamber OWC device is $R_{single} = 0.15$ m. The geometric parameters of the dual- and single- chamber OWC devices chosen for the experiment are summarized in Table 1. To monitor the free surface in the chambers, six wave gauges (i.e., G_2–G_7) were positioned to measure the instantaneous surface elevation as shown in Fig. 2(a). Two of the wave gauges (i.e., G_4 and G_5) were located in the inner chamber along the x-axis direction, and the others were symmetrically located about y-axis at intervals of 60 degrees in the outer chamber. In the present study, the wave gauges in each chamber were spatially located to average the free surface elevation. Two wave gauges G_1 (−0.525 m, 0 m, 0 m) and G_9 (−2.02 m, 0 m, 0 m) were set at the front side of the OWC to measure the wave reflected from the device. Wave gauge G_8 (−3.54 m, 0 m, 0 m) was set to measure the incident wave. As shown in Fig. 1, three pressure sensors (S_i, S_{o1} and S_{o2}) were used to record the air pressure in the chambers. The positions (x, y, z) of the pressure sensors are located at S_i (0 m, 0.07 m, 0.1 m), S_{o1}(−0.09 m, 0.2 m, 0.1 m) and S_{o2}(0.09 m, −0.2 m, 0.1 m). The average value of the pressure sensors S_{o1} and S_{o2} is regarded as the air pressure in the outer-chamber.

In the experiment, a range of regular wave conditions, as shown in Table 2, were generated in order to simulate scaled physical wave conditions. The wave period T is in the range of 1.1 s ≤ T ≤ 2.3 s, which represents full-scale waves with periods between 5 s and 10 s. The incident waves were generated with four different wave steepness kA (where k is the wave number, A is the wave amplitude), i.e., kA = 0.05, 0.075, 0.10 and 0.15.

2.2. Hydrodynamic efficiency

In order to study the energy transfer from the wave to the pneumatic air, the losses due to friction through the air orifice are ignored [46]. The air volume flux in the cylindrical chamber is represented by the averaged wave gauge values recorded in the chambers. Then, the wave power absorbed by the wave energy device (i.e., P_{owc}) in each chamber can be calculated from the measured air pressure p and air volume flux Q [47], as follows:

$$P_{owc} = \int_{S_f} p(t)\cdot Q(t)dS = \frac{S_f}{T}\int_t^{t+T} p(t)\cdot\bar{\dot{\eta}}(t)dt, \tag{1}$$

where S_f is the cross-sectional area of the free surface in the chamber, p is the air pressure in the chamber, η is the vertical elevation of the free surface in each chamber, $\dot{\eta}$ is the time rate of change of η, $\bar{\dot{\eta}}$ is calculated by averaging the wave gauge values in each chamber as follows:

$$\bar{\dot{\eta}} = \begin{cases} (\dot{\bar{\eta}}_{G4} + \dot{\bar{\eta}}_{G5})/2 & (in\ the\ inner\ chamber) \\ (\dot{\bar{\eta}}_{G2} + 2\dot{\bar{\eta}}_{G3} + 2\dot{\bar{\eta}}_{G6} + \dot{\bar{\eta}}_{G7})/6 & (in\ the\ outer\ chamber) \end{cases} \tag{2}$$

Based on linear wave theory, the average energy flux per unit width in the incident wave (i.e., P_{inc}) is

$$P_{inc} = \frac{\rho g A^2 \omega}{4k}\left(1 + \frac{2kh}{\sinh 2kh}\right), \tag{3}$$

where g is the gravitational acceleration, ρ is the water density and ω is the angular frequency which is determined according to the dispersion relationship $\omega^2 = gk\tanh(kh)$.

Thus, the hydrodynamic efficiency is defined as:

$$\mu = \frac{P_{owc}}{P_{inc}\cdot B_w}, \tag{4}$$

where B_w is the characteristic width of the water column. In this case, the characteristic width of the cylindrical OWC is taken as the diameter of the outer chamber.

2.3. Experimental repeatability

In order to minimize experimental uncertainties, experiments for each wave condition were repeated at least twice. The time series of the resulting data was analyzed in the regular oscillatory phase of the experiment. The time series record for air pressure and surface elevation in the inner and outer chambers at kh = 2.11(kA = 0.05) with d_1/h = 0.42, d_2/h = 0.3 and ε = 2.0% are shown in Figs. 3 and 4, respectively. It can be seen that both the air pressure and surface elevation for the repeated tests agree very well with each other. Fig. 4(a) and (b) show the whole time history of the surface elevation at gauge positions G_7 and G_8. These figures show that the waves reflected from the wave maker and from the absorbing beach are negligible and can be ignored. Hence, the experiments exhibit strong repeatability and stability.

3. Comparison between the experimental data and analytical solutions

Analytical techniques have been widely used in the preliminary hydrodynamic study of the cylindrical OWC devices based on linear potential flow theory and Eigen function expansion technique [48]. The present experimental results of the single-chamber OWC-WEC are

Table 2
Wave conditions.

T (s)	1.1	1.2	1.25	1.3	1.35	1.4	1.45	1.5	1.6	1.7	2.0	2.3
kh	3.33	2.81	2.6	2.42	2.26	2.11	1.99	1.87	1.68	1.53	1.2	1
A (mm) (kA = 0.05)	16.7	17.7	18.4	19.8	22.2	23.0	25.6	26.5	29.8	34.0	41.0	55.2
A (mm) (kA = 0.075)	–	–	29.9	–	33.2	35.0	39.8	–	–	–	–	–
A (mm) (kA = 0.10)	–	–	38.6	–	44.3	46.0	54.8	–	–	–	–	–
A (mm) (kA = 0.15)	–	–	55.7	–	66.2	71.2	78.4	–	–	–	–	–

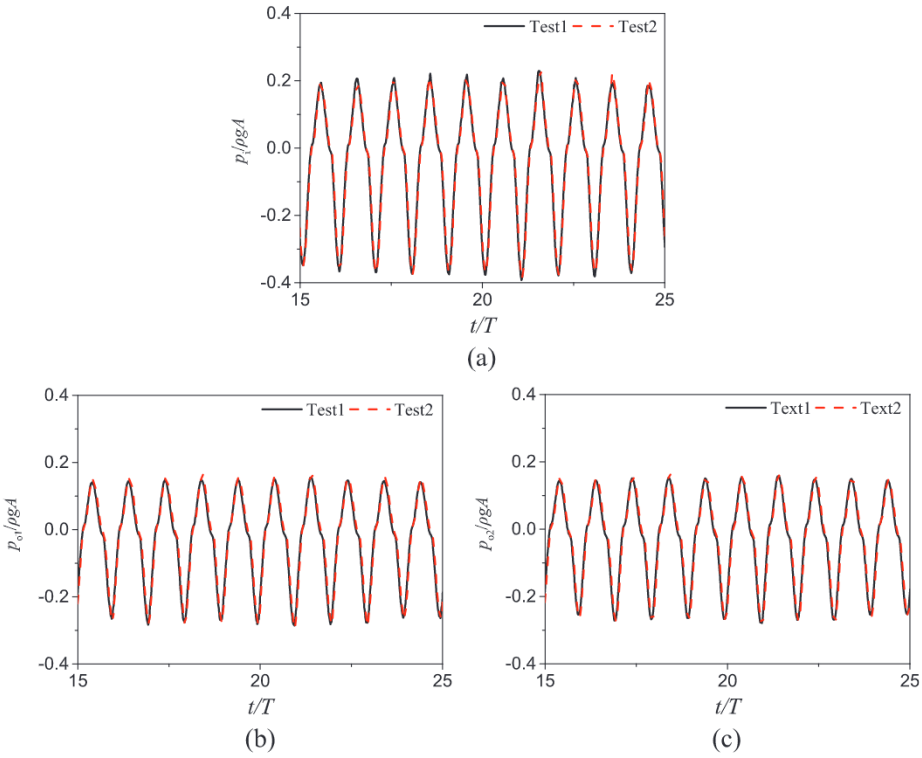

Fig. 3. Time series of air pressure at different positions for $kh = 2.11$. (a) S_i; (b) S_{o1}; (c) S_{o2}.

compared with the developed analytical solution [49] in this section. An incident wave with steepness $kA = 0.05$ is selected for the experimental investigation. The geometric parameters of the single-chamber OWC-WEC are set as $d_{single} = 0.42$ m, $b_{single} = 8$ mm and $R_{single} = 0.15$ m. The opening ratio of the single-chamber model is $\varepsilon = 2.0\%$. The chamber width $B_w = 0.3$ m in Eq. (4) is selected. The spring-like effect of air compressibility inside the chamber is neglected in both experimental and analytical models. Fig. 5 shows the comparisons between the analytical and experimental results for the hydrodynamic efficiency μ, and the air-pressure amplitude Δp. The air-pressure amplitude is defined as $\Delta p = [p(t)_{max} - p(t)_{min}]/2$. In order to model the turbine properties of the OWC device accurately, the parameter g_T in the analytical model is set as 1.82×10^{-4} m^5/N·s. This parameter characterizes the turbine damping [49]. The overall variations of the hydrodynamic efficiency and the chamber air-pressure amplitude given by the two methods show good agreement, especially for the prediction of the resonant frequency. It should be noted that the analytical solution overestimates the hydrodynamic efficiency around the resonant frequency, which is due to the viscous and nonlinear effects ignored in the analytical model.

4. Results and discussions

4.1. Variation of surface elevation in the chambers

The variation of the free surface elevation in the case of the dual-chamber OWC-WEC is considered in this section. Figs. 6 and 7 show the time series of the free surface elevation inside the chambers at $kh = 1.87(kA = 0.05)$ and $kh = 2.60(kA = 0.05)$, respectively. The geometric parameters of the dual-chamber OWC model are set as follows, $d_1/h = 0.42$, $d_2/h = 0.3$ and $\varepsilon = 2.0\%$. From Figs. 6 and 7, it can be seen that free surface elevations are always in phase inside the inner chamber, even though there is a slight phase difference recorded inside the outer chamber. The motion of the surface elevations leads to a near synchronous piston-type oscillation in both chambers. The wave amplitudes recorded at the various gauge locations with these geometric parameters are not exactly the same. This is more obvious for the short wavelength case as shown in Fig. 7(b). The wave amplitudes in the inner-chamber are smaller than those in the outer-chamber at $kh = 2.60$. Meanwhile, the wave amplitudes at gauges 6 and 7 are larger than those at gauges 2 and 3. This is because the short waves with weak penetrability are reflected by the inner-chamber shell and focused at the back of the outer chamber due to wave diffraction.

4.2. Comparison between the dual-chamber and single-chamber OWC devices

In this section, the hydrodynamic efficiency of the dual-chamber OWC device, in which only the inner-chamber is considered, is compared with that of the single-chamber device. The air-chamber heights in both the dual- and single- chamber devices are identically set as $d_c = 0.1$ m. The opening ratio $\varepsilon = 2.0\%$ is selected. The chamber drafts for the dual-chamber device are set to be $d_1 = 0.42$ m and $d_2 = 0.3$ m.

The efficiency spectra for the single-chamber OWC device and the inner-chamber with dimensionless wave number kh are shown in Fig. 8. The maximum efficiency of the inner-chamber is about 4% greater at the resonant frequency than that of the single-chamber device. This is because the existence of the outer-chamber shell enhances the performance of the inner-chamber OWC at the resonant frequency. In the high-frequency region (i.e., $kh > 2.5$), the hydrodynamic efficiency of the single-chamber is higher than that of the inner-chamber. The high-frequency wave with lower transmission ability is reflected by Shell-1 in the dual-chamber device, and then a proportion of wave energy cannot be absorbed by the inner-chamber. However, the effects of wave reflection from Shell-1 can be neglected in the low-frequency domain (i.e., $kh < 1.5$). It should be noted that there exists a significant discrepancy between the data sets at $kh = 1.53$. This may be due to the corresponding wavelength being close to the breadth of the wave flume. A transverse sloshing mode occurs at this wavelength due to the presence of the flume wall. This may reduce the wave energy capture ability of the dual-chamber OWC device in this study [23].

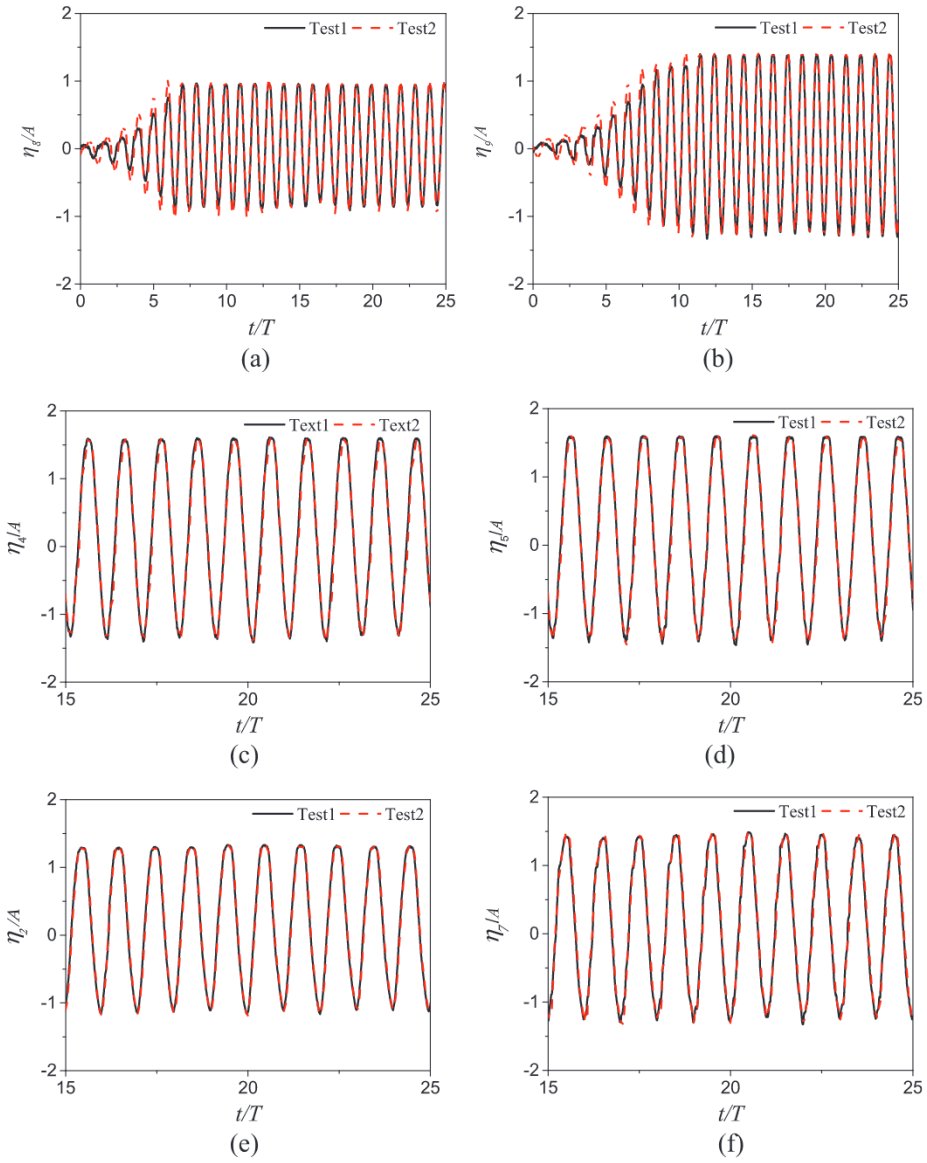

Fig. 4. Time series of surface elevation at different positions for $kh = 2.11$. (a) G_8; (b) G_9 (c) G_4; (d) G_5; (e) G_2; (f) G_7.

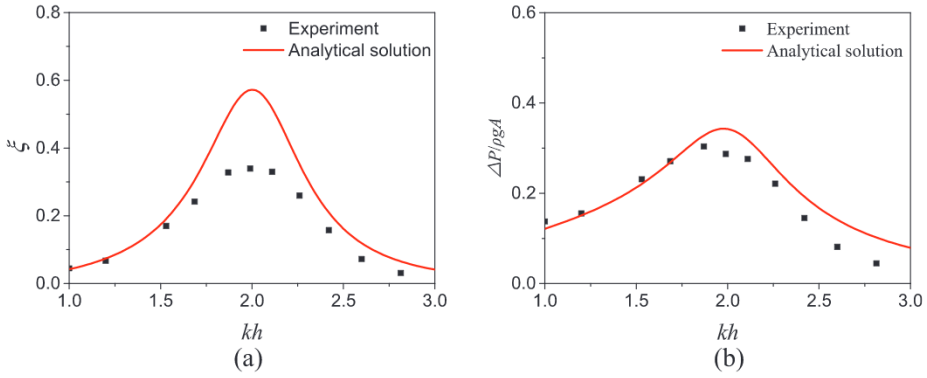

Fig. 5. Variation of experimental and analytical results of (a) hydrodynamic efficiency and (b) air-pressure amplitude with kh at $kA = 0.05$ and $\varepsilon = 2.0\%$.

4.3. Hydrodynamic performance inside the inner- and outer-chambers

In this section, the hydrodynamic performance inside the inner- and outer-chambers is discussed. An example with the parameters $d_1 = 0.42$ m, $d_2 = 0.3$ m, $d_c = 0.1$ m, $R_1 = 0.15$ m, $R_2 = 0.3$ m, $b_w = 0.1$ m and $\varepsilon = 2.0\%$ is considered. The wall thickness of Shell-1 is $b_{win} = 0.008$ m. Fig. 9 shows the time series of the amplitudes of the free surface elevation and air pressures with kh. In Fig. 9(a), the free surface oscillation amplitude η_A is the averaged difference between the crest and trough values (i.e., $\eta_A = (\eta_{crest} - \eta_{trough})/2$. In Fig. 9(b), the air

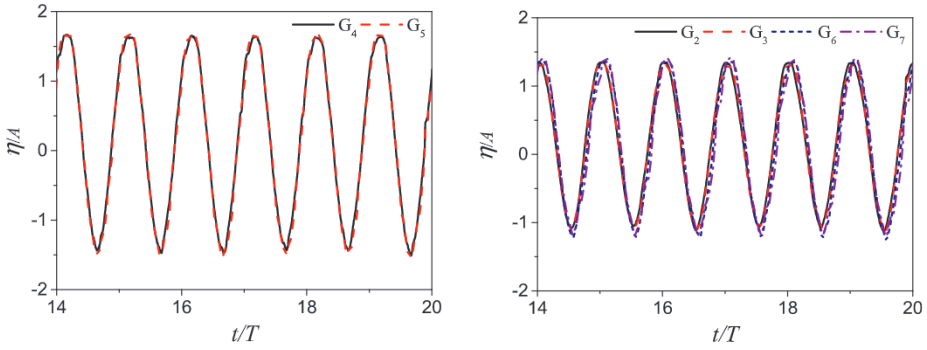

(a) Inside the inner chamber (b) Inside the outer chamber

Fig. 6. Time series of the surface elevation in the chambers at $kh = 1.87$.

pressure amplitude P_A is the averaged difference between the pressures of the crest and trough values ($P_A = (P_{crest} - P_{trough})/2$). In the low-frequency region ($kh < 1.50$), the dimensionless surface-elevation amplitude is near to unity and the air-pressure amplitudes recorded at the inner and outer chambers are almost identical. This is reasonable since the wave length in the low-frequency region is much larger than the chamber breadth. The scattering wave induced by the device can be ignored [50]. In the frequency range of $1.50 < kh < 2.25$, the amplitudes of the air pressure and surface elevation inside the inner-chamber are larger than those in the outer-chamber. This is because the inner-chamber has a larger chamber draft and smaller diameter, which leads to much stronger resonance effects as the water column oscillates in a narrower gap [51]. In this scenario, the fatigue damage to the inner chamber wall must be considered in engineering applications. From Fig. 9, it can also be seen that the maximum surface-elevation amplitudes in the chambers occur at the frequencies close to those corresponding to the maximum air-pressure amplitudes. This is because the maximum water oscillation velocity produces the peak air pressure in the chambers [52]. Compared with the amplitudes in the outer chamber, the amplitudes of the air pressure and surface elevation in the inner chamber decrease more rapidly in the high-frequency domain ($kh > 2.25$). This is consistent with high-frequency waves exhibiting low transmission ability, which can be easily reflected by the outer-chamber shell. Fig. 10 displays the distribution of total hydrodynamic efficiency ($\mu = \mu_{in} + \mu_{out}$, where μ_{in} *and* μ_{out} denote the hydrodynamic efficiency of the inner and outer chambers, respectively) of the different chambers with the dimensionless wave number kh. It is clear that the hydrodynamic efficiency of the outer chamber is greater than that of the inner chamber. This is because the cross-sectional area of the outer chamber is greater than that of the inner chamber. It can also be seen that the peak efficiencies of the inner and outer chambers occur at different incident wave frequencies, namely, $kh = 2.11$ and 2.42, respectively. These values also correspond to the resonant frequencies of

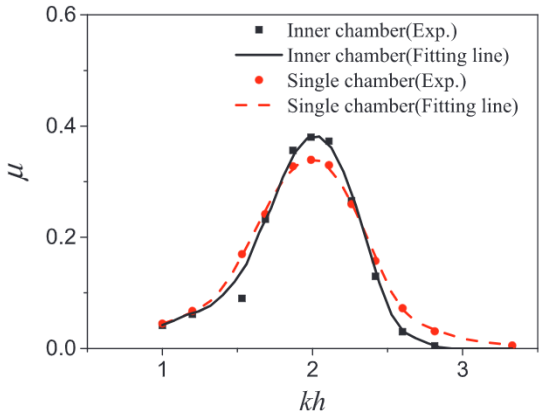

Fig. 8. Variation of hydrodynamic efficiency of the inner-chamber and the single-chamber OWC-WECs with kh at $kA = 0.05$ and $\varepsilon = 2.0\%$.

the air pressure and free surface elevation amplitudes as shown in Fig. 9. The effective frequency bandwidth of the whole OWC system can be broadened through the combination of two different chamber resonant frequencies. From these findings, it is recommended that such a dual-chamber OWC prototype can be deployed in the full-scale waves with the main periods between 5 s and 7 s to provide a hydrodynamic efficiency $\mu \geq 0.2$.

4.4. Effects of the opening ratios

In order to optimize the PTO system for the dual-chamber OWC-WEC, four different opening ratios ($\varepsilon = 1.0\%$, 1.5%, 2.0% and 3.0%) are investigated, as shown in Table 1. The chamber drafts for the dual-chamber device are set as $d_1 = 0.37$ m and $d_2 = 0.3$ m. The remaining parameters are set as $d_c = 0.1$ m, $b_{win} = 0.008$ m, $R_1 = 0.15$ m,

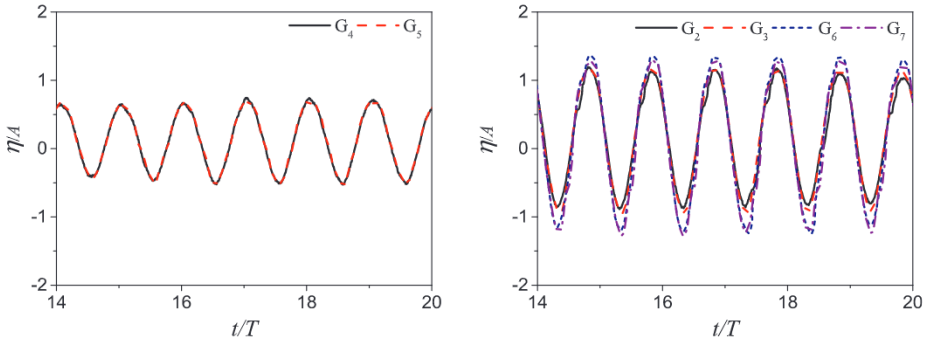

(a) Inside the inner chamber (b) Inside the outer chamber

Fig. 7. Time series of the surface elevation in the chambers at $kh = 2.60$.

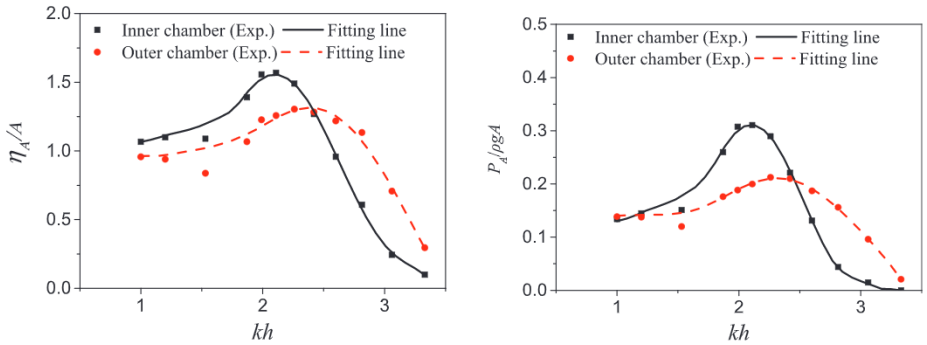

Fig. 9. Variations of the surface-elevation and air-pressure amplitudes with kh at $kA = 0.05$ and $\varepsilon = 2.0\%$.

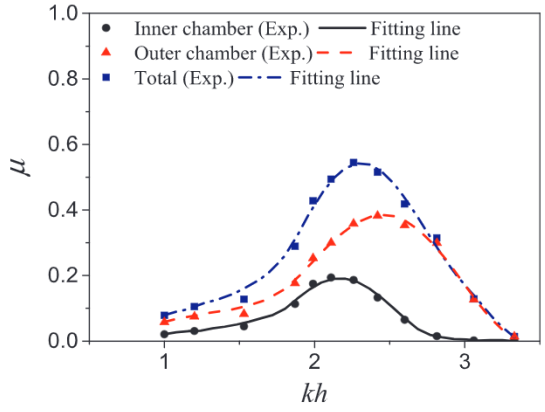

Fig. 10. Distribution of hydrodynamic efficiency μ of the inner chamber, outer chamber and whole OWC devices with kh at $kA = 0.05$ and $\varepsilon = 2.0\%$.

$R_2 = 0.3$ m and $b_w = 0.1$ m. The chamber width $B_w = 0.6$ m in Eq. (4) is selected. The incident wave number kh ranges from 1.00 to 3.33 with the constant wave steepness $kA = 0.05$.

The distributions of hydrodynamic efficiency for different air-orifice opening ratios are shown in Fig. 11. The hydrodynamic efficiencies for the total device ($\mu = \mu_{in} + \mu_{out}$) and the outer chamber μ_{out} reach the maximum when the opening ratio is between $\varepsilon = 1.5\%$ and 2.0% at the resonant frequency. A similar conclusion was ever obtained by Sheng et al. [39] in their experimental study on a floating cylindrical OWC-WEC. The optimal efficiency occurs at the resonant frequency with the orifice-opening ratio between 1.70% and 2.28% in their study. The orifice opening ratio for maximum efficiency occurs at $\varepsilon = 3.0\%$ in the inner chamber. The oscillating water column in the outer chamber enhances the hydrodynamic performance of the inner chamber when the opening ratio ε is less than 3.0%. Further investigation is needed to determine the optimal opening ratio of the inner chamber at the resonant frequency. In the low-frequency domain, it is clear that all the hydrodynamic efficiencies μ_{in}, μ_{out} and μ increase with greater turbine damping. This is because the long waves with a higher energy density can more easily transmit into the chambers. Hence, a large turbine damping value, which can generate a high air pressure, can enhance the hydrodynamic performance of the OWC-WEC in the low-frequency domain.

4.5. Effects of wave nonlinearity

The effects of wave nonlinearity on the hydrodynamic efficiency of the dual-chamber OWC device are investigated in this section. The experiments were conducted for four different wave conditions (i.e., $kh = 2.6$, 2.26, 2.11 and 1.99) with the OWC geometric parameters maintained at $d_1 = 0.37$ m, $d_2 = 0.30$ m, $b_{win} = 0.008$ m and $\varepsilon = 1.5\%$. Fig. 12 illustrates the influence of wave steepness kA ($kA = 0.05$, 0.075, 0.10 and 0.15) on the hydrodynamic efficiency μ versus dimensionless wave number kh. It is clear that the overall hydrodynamic efficiency decreases as the wave steepness kA increases. The effect of the wave nonlinearity on the hydrodynamic efficiency is more pronounced in the resonant frequency region compared with the high-frequency region. A similar phenomenon was also observed in the study of a land-fixed OWC device by Ning et al. [53]. They numerically and experimentally found that the peak efficiency decreases rapidly with an increase of wave amplitude. This suggests that the hydrodynamic efficiency of the OWC is strongly contingent on the degree of wave nonlinearity, especially in the resonant frequency domain. To further illustrate this phenomenon, the time series of wave elevations in the chambers are shown in Fig. 13. It can be observed that smaller wave amplitudes in the chambers are recorded for stronger incident waves. This is because the higher-order harmonic waves with shorter wave lengths can be more easily reflected by the chamber shell. Then, the capability to capture wave energy from the increasingly nonlinear waves is diminished.

4.6. Effects of the outer-chamber draft

The effects of the draft d_2 of Shell-2 on the hydrodynamic efficiency are discussed in this section. Fig. 14 presents the variation of the hydrodynamic efficiency of the complete system with three different drafts, i.e. $d_2 = 0.30$ m, $d_2 = 0.35$ m and $d_2 = 0.40$ m, while the remaining parameters $d_1 = 0.42$ m, $R_1 = 0.15$ m, $R_2 = 0.3$ m, $\varepsilon = 2.0\%$, $b_w = 0.1$ m and $kA = 0.05$ are kept constant. From the figure, it can be seen that the draft of Shell-2 has a significant effect on the total efficiency μ of the dual-chamber OWC device. With the decrease of the outer-chamber draft, the resonant frequency shifts to a higher frequency. The effective frequency bandwidth is broadened and can be observed to shift to the high-frequency region. The peak hydrodynamic efficiency of the dual-chamber OWC device increases and tends to stabilize at a maximum value. The reason for this phenomenon is that the wave energy can enter the chamber more easily for a shallower outer-chamber draft.

To further analyze the hydrodynamic properties of the dual-chamber OWC device, the hydrodynamic efficiency of the individual inner- and outer- chamber components are studied. Fig. 15 shows the distribution of hydrodynamic efficiency of the inner- and outer-chambers for different outer-chamber draft d_2. It is shown that both the effective frequency bandwidth and the resonant frequencies increase as the outer-chamber draft decreases. It should be noted that the draft of Shell-2 has a stronger influence on the hydrodynamic efficiency of the outer-chamber than that of the inner-chamber. This is attributed to the fact that wave energy density decreases greatly along the water depth increasing. Hence, this also means that a shallower outer-chamber draft can lead to a greater efficiency in the dual-chamber OWC system.

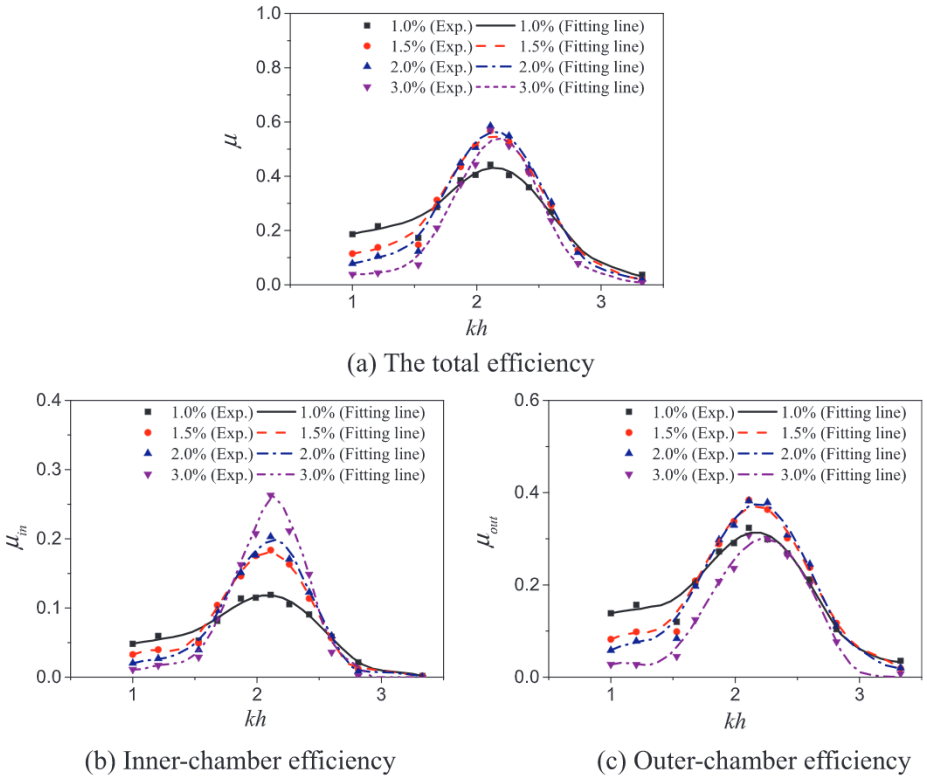

Fig. 11. Distributions of hydrodynamic efficiency μ for different opening ratios ε of the air orifice at $kA = 0.05$.

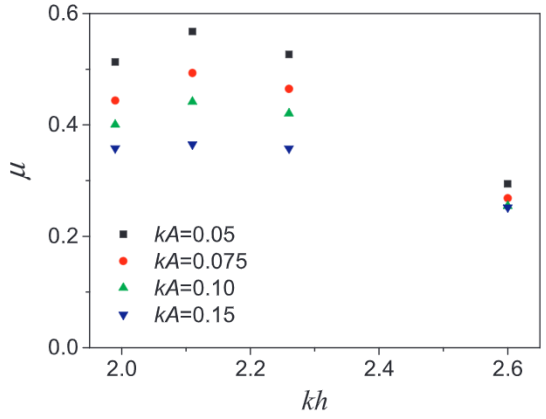

Fig. 12. Hydrodynamic efficiency μ versus dimensionless wave number for different kA at $\varepsilon = 1.5\%$.

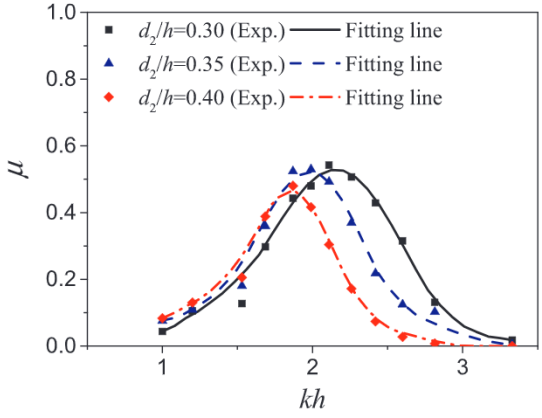

Fig. 14. Distribution of hydrodynamic efficiency μ for different draft d_2 at $kA = 0.05$ and $\varepsilon = 2.0\%$.

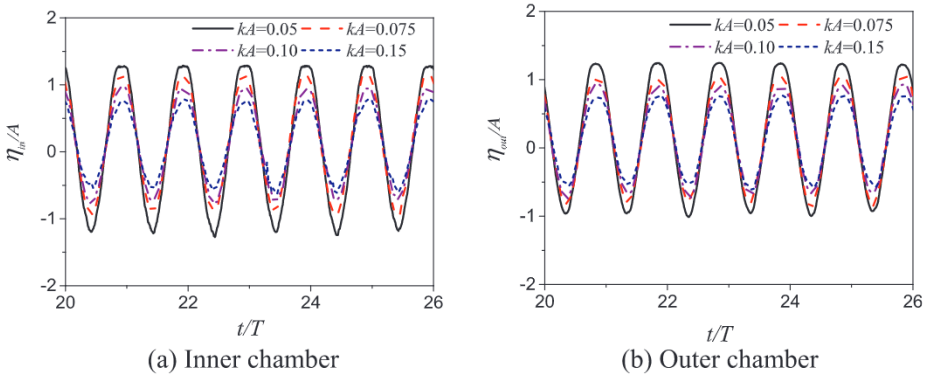

Fig. 13. Time series of the averaged surface elevation in the chambers for different kA at $\varepsilon = 1.5\%$.

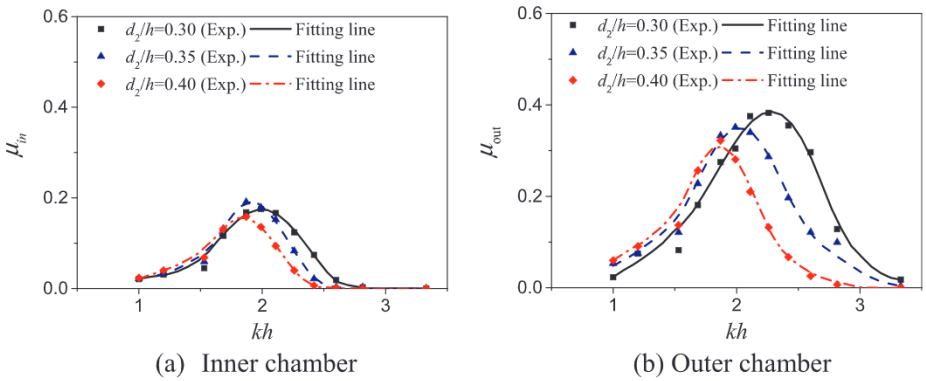

Fig. 15. Distribution of hydrodynamic efficiency of (a) inner chamber and (b) outer chamber for different draft d_2 at $kA = 0.05$ and $\varepsilon = 2.0\%$.

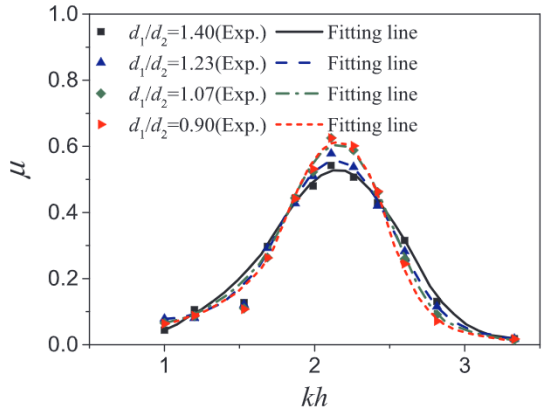

Fig. 16. Distribution of the total hydrodynamic efficiency μ for different draft d_1 at $kA = 0.05$ and $\varepsilon = 2.0\%$.

4.7. Effects of the inner-chamber draft variation

The variation of the hydrodynamic efficiency resulting from different inner-chamber draft is discussed in this section. Fig. 16 shows the distribution of the total hydrodynamic efficiency of the dual-chamber OWC device with the experiment parameters set to be $d_2 = 0.3$ m, $R_1 = 0.15$ m, $R_2 = 0.3$ m, $\varepsilon = 2.0\%$, $b_w = 0.1$ m and $kA = 0.05$. Four different drafts of Shell-1 are examined, i.e., $d_1 = 0.42$ m ($d_1/d_2 = 1.4$), $d_1 = 0.37$ m ($d_1/d_2 = 1.23$), $d_1 = 0.32$ m ($d_1/d_2 = 1.07$), and $d_1 = 0.27$ m ($d_1/d_2 = 0.9$). From the figure, it can be observed that the hydrodynamic efficiency increases slightly with the increase of the inner-chamber draft in the high-frequency region. This is due to the wave reflection from Shell-1 enhancing the energy capture ability of the outer-chamber device. The effective frequency bandwidth increases as the inner-chamber draft increases, even though the peak efficiency reduces. It should be noted that the peak efficiency varies slightly for the cases $d_1 = 0.32$ m and $d_1 = 0.27$ m. Hence, the influence of the inner-chamber draft on the peak efficiency of the proposed dual-chamber OWC device diminishes when the inner-chamber draft is smaller than the outer-chamber draft. In the low-frequency domain, the hydrodynamic efficiency is not sensitive to variation of the inner-chamber draft due to long wave effects.

Fig. 17 shows the variation of the hydrodynamic efficiency of the inner- and outer- chamber components with kh for different inner-chamber drafts. From Fig. 17(a), it can be seen that the resonant frequency shifts to low-frequency region as the inner-chamber draft increases. For a deeper inner- chamber draft, only the long waves contribute noticeably at the resonance. The influence of the draft of Shell-1 on the hydrodynamic efficiency of the outer-chamber is smaller than that of Shell-2 as shown in Fig. 15. This is in contrast to the effects of the draft of the inner chamber. This can be clearly observed in the low-frequency domain. In the high-frequency domain, the hydrodynamic efficiency of the inner-chamber decreases as the inner-chamber draft increases. However, the hydrodynamic efficiency of the outer-chamber increases as shown in Fig. 17(b). This is due to the wave reflection from Shell-1, leading to a higher hydrodynamic efficiency in the high-frequency region. From Figs. 16 and 17, it can be concluded that the dual-chamber OWC system with a larger inner-chamber draft can broaden the effective frequency bandwidth, even though the resonant hydrodynamic efficiency reduces slightly.

5. Conclusions

In this study, the hydrodynamic properties of a 3D stationary cylindrical OWC-WEC with dual-chamber is investigated through a series of wave tests. The dual-chamber OWC model experiment was carried out to explore the influence of wave nonlinearity and various chamber geometric parameters on the hydrodynamic efficiency, water motion and air pressure inside the chambers. The overall variation trends of the observed chamber air-pressure and the hydrodynamic efficiency in the case of the single-chamber OWC device agree well with the published analytical solutions.

There exist two different resonant frequencies corresponding to the inner- and outer- chambers. Their combination can broaden the effective efficiency bandwidth of the dual-chamber OWC system. The PTO systems were simulated by incorporating circular orifices with different opening ratios. It was found that the optimal peak hydrodynamic efficiency for the present OWC model occurs with an opening ratio ε being between 1.5% and 2.0%.

In the dual-chamber OWC device, the introduction of the outer-chamber shell can increase the hydrodynamic efficiency of the inner-chamber component by comparison with the single-chamber OWC device. The incident waves with different wave steepness kA were generated to investigate the nonlinear effect on the hydrodynamic efficiency. In the case of stronger wave nonlinearity, lower hydrodynamic efficiency can be obtained. The effects of the drafts of Shell-2 and Shell-1 on the hydrodynamic performance was studied. It was found that the dual-chamber OWC device with the deep inner-chamber draft broadens the effective frequency bandwidth, even though the resonant hydrodynamic efficiency reduces. The dual-chamber OWC device with the relative shallow outer-chamber draft yields a high efficiency.

This experimental study on the cylindrical dual-chamber OWC device can be used as a guide for the geometrical design of such systems. Future work will focus on developing a nonlinear numerical model of the dual-chamber cylindrical OWC device. Then the model can be used to extensively simulate and investigate the hydrodynamic loads on the OWC systems and their durability. Furthermore, the present experimental work can be used as a benchmarking validation for various numerical models.

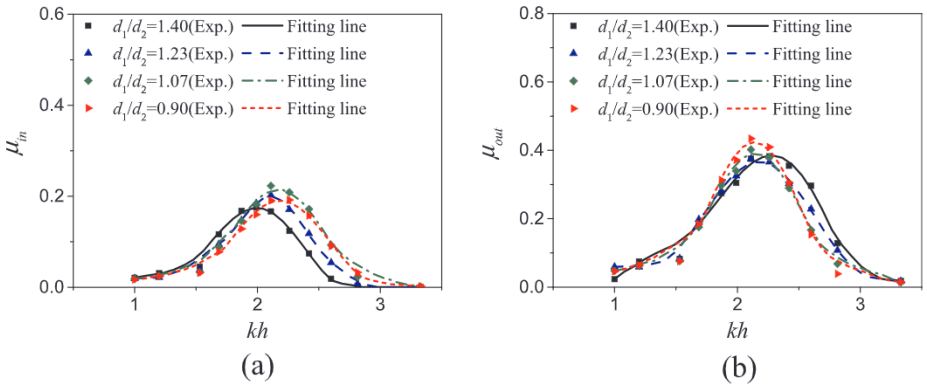

Fig. 17. Distribution of hydrodynamic efficiency of the (a) inner-chamber and (b) outer-chamber for different draft d_1 at $kA = 0.05$ and $\varepsilon = 2.0\%$.

Author contributions

Experimental tests and result analyses were conducted by D.N., Y.Z. and R.M. Comments and suggestions by L.J. All authors reviewed the manuscript.

Declaration of Competing Interest

The authors declare no conflict of interest.

Acknowledgements

This work is supported by the National Key R&D Program of China (Grant No. 2018YFB151905), National Natural Science Foundation of China (Grant Nos. 51679036 and 51761135011) and EPSRC project (Grant No. EP/R007519/1).

Appendix A. Supplementary material

Supplementary data to this article can be found online at https://doi.org/10.1016/j.apenergy.2019.114252.

References

[1] Capellán-Pérez I, Mediavilla M, Castro C, Carpintero Ó, Miguel LJ. Fossil fuel depletion and socio-economic scenarios: an integrated approach. Energy 2014;77:641–66.
[2] Leonard MD, Michaelides EE, Michaelides DN. Energy storage needs for the substitution of fossil fuel power plants with renewables. Renew Energy 2020;145:951–62.
[3] Johannes F. A review of wave-energy extraction. Mar struct 2007;20(4):185–201.
[4] Borthwick AG. Marine renewable energy seascape. Engineering 2016;2:69–78.
[5] Zhang X, Tian X, Xiao L, Li X, Chen L. Application of an adaptive bistable power capture mechanism to a point absorber wave energy converter. Appl Energy 2018;228:450–67.
[6] Falcão AFO. Wave energy utilization: a review of the technologies. Renew Sust Energ Rev 2010;14:899–918.
[7] Heath TV. A review of oscillating water columns. Philos Trans R Soc A 2012;370:235–45.
[8] Evans DV. The oscillating water column wave-energy device. IMA J Appl Math 1978;22(4):423–33.
[9] Falcão AFO. The shoreline OWC wave power plant at the Azores. In: 4th European wave energy conference. Aalborg, Denmark; 2000. p. 42–8.
[10] Falcão AFO, Henriques JCC. Oscillating-water-column wave energy converters and air turbines: a review. Renew Energy 2016;85:1391–424.
[11] Healt T, Whittaker T, Boake C. The design, construction and operation of the LIMPET wave energy converter (Islay, Scotland). In: 4th European wave energy conference. Aalborg, Denmark; 2000. p. 49–55.
[12] Zhang D, Li W, Lin Y. Wave energy in China: current status and perspectives. Renew Energy 2009;34:2089–92.
[13] Henriques JCC, Portillo JCC, Sheng W, Gato LMC, Falcao AFO. Dynamics and control of air turbines in oscillating-water-column wave energy converters: analyses and case study. Renew Sust Energ Rev 2019;112:571–89.
[14] Garrett CJR. Bottomless harbours. J Fluid Mech 2006;43:433–49.
[15] Sarmento AJNA, Falcão AFO. Wave generation by an oscillating surface-pressure and its application in wave-energy extraction. J Fluid Mech 1985;150:467–85.
[16] Evans DV, Porter R. Efficient calculation of hydrodynamic properties of OWC-type devices. J Offshore Mech Arct 1997;119(4):210–8.
[17] Zheng S, Zhang Y, Iglesias G. Coast/breakwater-integrated OWC: a theoretical model. Mar Struct 2019;66:121–35.
[18] Zheng S, Antonini A, Zhang Y, Greaves D, Miles J, Iglesias G. Wave power extraction from multiple oscillating water columns along a straight coast. J Fluid Mech 2019;878:445–80.
[19] Martins-Rivas H, Mei CC. Wave power extraction from an oscillating water column along a straight coast. Ocean Eng 2009;36:426–33.
[20] Rezanejad K, Bhattacharjee J, Soares CG. Stepped sea bottom effects on the efficiency of nearshore oscillating water column device. Ocean Eng 2013;70:25–38.
[21] Deng Z, Huang Z, Law AWK. Wave power extraction from a bottom-mounted oscillating water column converter with a V-shaped channel. P Roy Soc A – Math Phy 2014;470(2167):20140074.
[22] Ning DZ, Zhou Y, Zhang C. Hydrodynamic modeling of a novel dual-chamber OWC wave energy converter. Appl Ocean Res 2018;78:180–91.
[23] Nader JR, Zhu SP, Cooper P, Stappenbelt B. A finite-element study of the efficiency of arrays of oscillating water column wave energy converters. Ocean Eng 2012;43:72–81.
[24] Gomes RPF, Henriques JCC, Gato LMC, Falcão AFO. Wave power extraction of a heaving floating oscillating water column in a wave channel. Renew Energy 2016;99:1262–75.
[25] Ning DZ, Wang RQ, Chen LF, Sun K. Experimental investigation of a land-based dual-chamber owc wave energy converter. Renew Sust Energ Rev 2019;9:48–60.
[26] López I, Pereiras B, Castro F, Iglesias G. Optimisation of turbine-induced damping for an OWC wave energy converter using a RANS–VOF numerical model. Appl Energy 2014;127:105–14.
[27] Elhanafi A, Macfarlane G, Fleming A, Leong Z. Scaling and air compressibility effects on a three-dimensional offshore stationary OWC wave energy converter. Appl Energy 2017;189:1–20.
[28] Xu CH, Huang ZH. Three-dimensional CFD simulation of a circular OWC with a nonlinear power-takeoff: model validation and a discussion on resonant sloshing inside the pneumatic chamber. Ocean Eng 2019;176:184–98.
[29] Çelik A, Altunkaynak A. Determination of damping coefficient experimentally and mathematical vibration modelling of OWC surface fluctuations. Renew Energy 2020;147:1909–20.
[30] Wilbert R, Sundar V, Sannasiraj SA. Wave interaction with a double chamber oscillating water column device. Int J Ocean Climate Syst 2013;4(1):21–39.
[31] Moretti G, Rosati Papini GP, Daniele L, Forehand D, Ingram D, Vertechy R, et al. Modelling and testing of a wave energy converter based on dielectric elastomer generators. Proc R Soc A 2019;475:20180566.
[32] Pawitan KA, Dimakopoulos AS, Vicinanza D, Allsop W, Bruce T. A loading model for an OWC caisson based upon large-scale measurements. Coast Eng 2019;145:1–20.
[33] Xu C, Huang Z, Deng Z. Experimental and theoretical study of a cylindrical oscillating water column device with a quadratic power take-off model. Appl Ocean Res 2016;57:19–29.
[34] Mahnamfar F, Altunkaynak A. Comparison of numerical and experimental analyses for optimizing the geometry of OWC systems. Ocean Eng 2017;130:10–24.
[35] Zhao XL, Ning DZ, Zou QP, Qiao DS, Cai SQ. Hybrid floating breakwater-WEC system: a review. Ocean Eng 2019;186:106–26.
[36] Elhanafi A, Fleming A, Macfarlane G, Leong Z. Numerical hydrodynamic analysis of an offshore stationary–floating oscillating water column–wave energy converter using CFD. Int J Nav Archit Ocean Eng 2017;9:77–99.
[37] Falcão AFO, Henriques JCC. The spring-like air compressibility effect in oscillating-water-column wave energy converters: review and analyses. Renew Sust Energ Rev 2019;112:483–98.
[38] He F, Huang ZH, Law AWK. An experimental study of a floating breakwater with asymmetric pneumatic chambers for wave energy extraction. Appl Energy 2013;106:222–31.
[39] Sheng W, Brian F, Anthony L, Raymond A. Experimental studies of a floating cylindrical OWC WEC. In: ASME 2012 31st international conference on ocean, offshore and arctic engineering. Rio de Janeiro(Brazil): Ocean, Offshore and Arctic Engineering Division; 2012:169–78.
[40] Elhanafi A, Macfarlane G, Fleming A, Leong Z. Experimental and numerical investigations on the hydrodynamic performance of a floating–moored oscillating

water column wave energy converter. Appl Energy 2017;205:369–90.
[41] Correia DFFX, Gomes RPF, Henriques JCC, Gato LMC, Falcão AFO. Model testing of an oscillating water column spar-buoy wave energy converter isolated and in array: motions and mooring forces. Energy 2016;112:1207–18.
[42] Louise O, Björn E, Trevor W. Experimental measurement of wave field variations around wave energy converter arrays. Sustainability 2017;9(1).
[43] Zhou Y, Ning DZ, Wang RQ. Experimental study on a 3D offshore-stationary dual-chamber OWC wave energy converter. In: Proceedings of the twenty-ninth international ocean and polar engineering conference. (Honolulu, Hawaii, USA) 2019;1:140–5.
[44] Charkabarti S. Offshore structure modeling. World Scientific; 2015.
[45] Falcao AFO, Henriques JCC. Model-prototype similarity of oscillating-water-column wave energy converters. Int J Mar Energy 2014;6:18–34.
[46] Wang R, Ning D, Zhang C. Nonlinear and viscous effects on the hydrodynamic performance of a fixed OWC wave energy converter. Coast Eng 2018;131:42–50.
[47] Ning DZ, Shi J, Zou QP, Teng B. Investigation of hydrodynamic performance of an OWC (oscillating water column) wave energy device using a fully nonlinear HOBEM (higher-order boundary element method). Energy 2015;83:177–88.
[48] Martins-Rivas H, Mei CC. Wave power extraction from an oscillating water column at the tip of a breakwater. J Fluid Mech 2009;626:395–414.
[49] Mavrakos SA, Konispoliatis DN. Hydrodynamics of a free floating vertical axisymmetric oscillating water column device. J Appl Math 2012;3:2603–21.
[50] Zhou Y, Zhang C, Ning DZ. Hydrodynamic investigation of a concentric cylindrical OWC wave energy converter. Energies 2018;11:985.
[51] Lu L, Teng B, Cheng L, Sun L. Modelling of multi-bodies in close proximity under water waves—fluid resonance in narrow gaps. Sci. China 2011;54(1):16–25.
[52] Iturrioz A, Guanche R, Lara JL. Validation of OpenFOAM for oscillating water column three-dimensional modeling. Ocean Eng 2015;107:222–36.
[53] Ning DZ, Wang RQ, Zou QP. An experimental investigation of hydrodynamics of a fixed OWC wave energy converter. Appl Energy 2016;168:636–48.